Journal of Materials Chemistry A

Accepted Manuscript

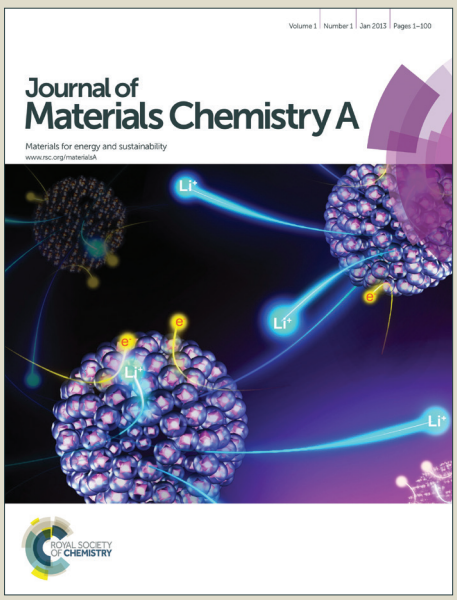

ROYAL SOCIETY OF CHEMISTRY

www.rsc.org/materialsA

Journal Name

RSCPublishing

ARTICLE

Ionic transport through a composite structure of *N*-ethyl-*N*-methylpyrrolidinium tetrafluoroborate organic ionic plastic crystals reinforced with polymer nanofibres

Cite this: DOI: 10.1039/xoxxoooooox

Received ooth January 2012,
Accepted ooth January 2012

DOI: 10.1039/xoxxoooooox

www.rsc.org/

N. Iranipour[a], D. J. Gunzelmann[b], A. Seeber[c], J. Vongsvivut[b], C. Doherty[c], F. Ponzio[a], L. A. O'Dell[b], A. F. Hollenkamp[a,c], M. Forsyth[a] and P. C. Howlett[a,*]

The incorporation of Polyvinylidene difluoride (PVDF) electrospun nanofibres within *N*-ethyl-*N*-methylpyrrolidinium tetrafluoroborate, [C_2mpyr][BF_4] was investigated with a view to fabricating self-standing membranes for various electrochemical device applications, in particular lithium metal batteries. Significant improvement in mechanical properties and ionic conduction was demonstrated in a previous study, which also demonstrated the remarkably high performance of the lithium-doped composite material in a device. We now seek a fundamental understanding of the role of fibres within the matrix of the plastic crystal, which is essential for optimizing device performance through fine-tuning of the composite material properties. The focus of the current study is therefore a thorough investigation of the phase behaviour and conduction behaviour of the pure and the lithium-doped (as $LiBF_4$) plastic crystal, with and without incorporation of polymer nanofibres. Analysis of the structure of the plastic crystal, including the effects of lithium ions and the incorporation of PVDF fibres, was conducted by means of synchrotron XRD. Ion dynamics were evaluated using VT solid-state NMR spectroscopy. ATR-FTIR spectroscopy was employed to gain insights into the molecular interactions of doped lithium ions and/or the PVDF nanofibres in the matrix of the [C_2mpyr][BF_4] composites. Preliminary measurements using PALS were conducted to probe structural defects within the pure materials. It was found that ion transport within the plastic crystal was significantly altered by doping with lithium ions due to the precipitation of a second phase in the structure. The incorporation of the fibres activated more mobile sites in the systems, but restricted ion mobility with different trends were observed for each ion species in each crystalline phase. In the presence of the fibres a strong interaction observed between the Li ion and the pyrrolidinium ring disappeared and formation of the second phase was prevented. As a result, an increased number of mobile lithium ions are released into the solid solution structure of the matrix, simultaneously removing the blocking effect of the second phase. Thus, ion conduction was remarkably improved within the Li-doped composite compared to the neat Li-doped plastic crystal.

Introduction

As a class of materials, organic ionic plastic crystals (OIPCs) often possess both high electrochemical and thermal stability which, together with unusually high solid-state ionic conductivity, makes them promising electrolyte materials for the next generation of safe, high specific energy lithium batteries[1-5]. OIPCs have these unique properties because they can exist in several distinct solid phases at temperatures below the melting point. In essence, OIPCs disorder in a staged manner, over a relatively broad temperature range, within which, the material passes through one or more plastic phase transitions finally approaching the melt. While a long range crystalline ordering is maintained up to the melting point, each plastic phase transition is accompanied by progressive increases in localized orientational, conformational and/or rotational disorder. With each increase in disorder, new modes of ion movement become accessible, which explains why OIPCs can show high ionic conductivities in the solid state[6]. The plastic nature of OIPCs, due to the presence of mobile defects, such as slip planes and dislocations, is desirable for electrochemical device fabrication.

When an OIPC is mixed with inorganic ions (such as lithium /sodium salts for battery applications or I^-/I_3^- for dye-sensitized

solar cells), the rotational motions of the ion species can facilitate the transport of specific 'target' ions in the structure. For example, MacFarlane et al. demonstrated 20 times increase in ionic conductivity of the slightly conductive [C_1mpyr] and [C_2mpyr] compounds at 25°C by mixing with less than 1% Li ion[7-11]. Structural defects such as vacancies and slip planes, provide additional assistance for target ion diffusion[12, 13]. A few studies have reported facilitation of ion transport and conduction through defect formation and introduction of disorder in the OIPC structure[14-16]. For example, reports of improvement in the ion conductivity upon incorporation of ceramic nano-particles into the matrix of OIPCs suggested increased disorder within the structure of the OIPC was the dominant mechanism, without providing further structural analysis of the resultant composite materials[16-19].

The chemical and mechanical stability of polymer nanofibres as separators in lithium batteries has been demonstrated in several studies. Satisfactory electrochemical performance of the materials was reported when soaked with organic carbonate solvents or ionic liquids as electrolytes[20-24]. Polyvinylidene difluoride (PVDF) nanofibres have been widely used as separators in lithium battery technology with reportedly an improved cell performance compared to the relevant commercial materials[23].

Here we sought to combine the beneficial effects of OIPCs as highly conductive solid-state electrolytes with the relatively high mechanical strength and chemical durability of polymer nanofibres by bringing them together to make composite electrolyte membranes. The incorporation of polymer fibres into the OIPC matrix provides mechanical support, helping in the fabrication of self-standing flexible thin membranes, thereby offering significant improvement in the mechanical properties of the OIPC. It was hypothesized that incorporation of fibres would also introduce disorder and defects, and thus assist ionic transport through the OIPC structure. Indeed, an earlier study showed that incorporating fibres improved the ionic conduction of lower-temperature lithium-doped plastic crystalline phases to the point where lithium ion cell cycling could be demonstrated[25].

The focus of the current work is a detailed study of the thermal and conduction behaviour of the pure and lithium-doped OIPCs in the neat state and also when cast into nanofibre networks. We have chosen to study the OIPC *N*-ethyl-*N*-methyl pyrrolidinium tetrafluoroborate [C_2mpyr][BF_4] due to its broad plastic crystal range, and its composites with PVDF electrospun nanofibres, with and without the addition of $LiBF_4$. The structure, dynamics and vibrational behaviour of the ionic species within the various phases of the OIPC and composites, and how these change with doping and incorporation of fibres are described. Thorough understanding of the role of fibres in ionic transport within the membrane is needed so that the properties of the membrane can be tuned for optimum performance as flexible, solid-state electrolytes in the next developments of lithium battery technology.

Methodology

The thermal behaviour of the materials was analysed using differential scanning calorimetry (DSC). The crystal structures were investigated at different phases using Synchrotron X-ray powder diffractometry (XRD). The mobility of ion species was probed through variable temperature, VT solid-state nuclear magnetic resonance spectroscopy (NMR). The molecular bonding and interactions were further analysed through vibrational spectral features obtained using attenuated total reflectance Fourier transform infrared (ATR-FTIR) spectroscopy. Positron annihilation lifetime spectroscopy (PALS) was used to probe structural defects within the pure OIPC.

Materials

N-ethyl-*N*-methylpyrrolidinium tetrafluoroborate [C_2mpyr][BF_4] (98%) was purchased from io-li-tec. The OIPC was purified by recrystallization from dry acetonitrile (Merck) in two steps: precipitation for 24 h in a refrigerator at 4°C and stirring for 24 h in the presence of activated carbon at room temperature. The filtered solid from both steps was dried under reduced pressure for 48 h. Lithium tetrafluoroborate, $LiBF_4$ (99.998%) was purchased from Sigma Aldrich and used as received. The pure OIPC was mixed with 10 mol% $LiBF_4$ by dissolving both materials in dried acetonitrile (Merck) and mixing for 4 h under a nitrogen atmosphere. The solvent was removed using a rotary evaporator followed by keeping in high vacuum at 50°C for 24 h. The concentration used here was chosen according to previous work on optimizing the ionic conductivity of the OIPC doped with various concentrations of the lithium salt[26]. PVDF granules were purchased from Sigma Aldrich. Electrospinning was applied to a homogenous solution of 20 g PVDF granules in a 100 ml mixture of dimethylformamide (DMF) and acetone (4:6 v/v), using a KD Scientific pump with a flow rate of 1 ml/h. The applied voltage was 16 kV and the distance between the syringe tip and the collector was 15 cm. Both pure and lithium-doped OIPCs were introduced into the nanofibre mat by casting of the OIPCs dissolved in acetone (HPLC grade, Scharlau). The detailed procedures for the preparation of the composite material were previously reported elsewhere[25].

The chemical structures of [C_2mpyr][BF_4] and PVDF are illustrated in figure 1.

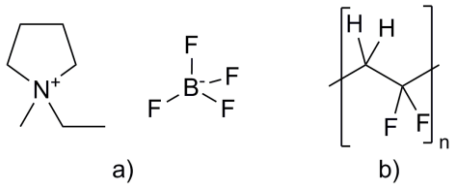

Figure 1. Chemical structures of a) N-ethyl-N-methylpyrrolidinium tetrafluoroborate [C_2mpyr][BF_4] and b) Polyvinylidene difluoride, PVDF.

Thermal analysis

A Mettler Toledo differential scanning calorimeter (DSC) was used for thermal analysis between -100°C and 130°C at a scan rate of 10°Cmin^{-1}. All samples were held at -80°C for 20 min and at -100°C for 5 min during the cooling step before heating. The reported traces are for the heating step. All sample preparation and sealing of the pans was conducted inside an argon glove box. Heat flow of the materials was normalized to the mass of plastic crystal within each sample.

Electrochemical impedance spectroscopy (EIS)

Solid-state ionic conductivity of the materials was evaluated using electrochemical impedance spectroscopy on a Bio-logic SP-200 potentiostat driven by EC-lab V10.12 software. Pellets of the pre-dried pure and lithium-doped samples were pressed inside a KBr die under 3.5 tons pressure. The composite samples were prepared as described in the material preparation section. All samples after pressing were dried for 24 h at 55°C inside a vacuum oven. The samples were sandwiched between pre-polished and dried circular stainless steel electrodes located inside hermetically-sealed barrel cells (Advanced Industrial Services, Moorabbin, Australia). All material handling was carried out inside an argon glove box. A tubular Helios furnace (28V/32W) with a flexible ceramic heater was used to apply the temperature ramp. A Eurotherm 3504 temperature controller interfaced to the potentiostats, allowed impedance data to be acquired automatically throughout a programmed temperature profile. A T type thermocouple with an accuracy of ±1°C was used for the temperature measurements. The temperature stabilization time between measurements was 20 min, at 10°C intervals. Data were collected at each temperature by applying a sinusoidal signal with amplitude of 200 mV over a frequency range of 5 MHz – 100 mHz. Conductivity values were calculated from Nyquist plots in which the touchdown point of the semicircle corresponds to the bulk resistance of the ionic conducting media. Activation energy of all materials in each phase was calculated according to following equation[27]:

$$\sigma = \sigma_0 \exp \frac{-E_a}{RT} \quad (1)$$

In which σ is ionic conductivity in Scm^{-1}, σ_0 is a pre-exponential factor, R is the gas constant in J mol^{-1} K^{-1}, T is temperature in K and E_a is activation energy in J mol^{-1} .

Synchrotron X-ray diffractometry (XRD)

Variable temperature XRD was conducted on pure and lithium doped OIPCs and the PVDF composites at the powder diffraction beam line at the Australian Synchrotron. An array of 16 MYTHEN ID microstrip silicon detectors with each module spanning about 5 degrees in 2Θ covered data collection over the angular range from ~3° to 83°. All samples were packed into 0.3 mm borosilicate glass capillaries (supplied by Charles Supper Company, Massachusetts, USA) inside a controlled atmosphere (argon) glovebox. The calibration was made with respect to 5 min acquired data on the NIST 660b LaB_6 reference material. The wavelength was set at 1.001295 Å using a Si (111) double crystal monochromator prior to data collection. The temperature was controlled within 0.1-0.2°C of the set point for all measurements using a Cyberstar hot-air blower. A 5°Cmin^{-1} temperature ramp rate was applied prior to temperature equilibration for 10 min for all samples. The data were acquired for 5 min for the pure OIPC and 7.5 min for the lithium doped OIPC for each of the two detector settings. For each of the two detector settings, the acquisition duration for both pure and lithium doped PVDF composites was 10 min for the low temperature measurement (-80°C) and 5 min for the high temperature measurements (50°C, 100°C). The data acquired from each detector setting was merged into a single set for each material and the patterns plotted from the merged data thus obtained. The numbers of ion pairs filling each unit cell was calculated by assuming the density of the pure material according to the previous studies [28-30]. Accordingly, the theoretical density of the materials was calculated by considering the total mass of the reported ion pairs occupying the volume of each unit cell.

Solid-state nuclear magnetic resonance (NMR) spectroscopy

Solid-state NMR spectra were recorded on a Bruker Avance III spectrometer, operating at 7.05 T, at Larmor frequencies of 300.13, 272.8 and 116.6 MHz for ^{1}H, ^{19}F and ^{7}Li, respectively. All ^{1}H chemical shifts are given relative to TMS, all ^{19}F shifts are referenced to CCl_3F, and ^{7}Li shifts are relative to a 1 M LiCl aqueous solution. All samples were prepared and packed into 2.5 mm or 4 mm zirconia MAS rotors in a glove box. The packed rotors were loaded into Bruker solid-state NMR probes and measured at varying temperatures starting at 20°C. Between each temperature step samples were equilibrated for 15-30 min. Temperature was calibrated using $Pb(NO_3)_2$ to be precise within ± 2°C[31].

The collected spectra were analysed using DMfit software[32]. Extracted ^{7}Li line width values were plotted against temperature and the correlation time for Li ions was calculated by fitting of the curves according to the following equation[33]:

$$(\Delta\nu)^2 = \frac{2}{\pi}\,\delta\omega_0^2 \tan^{-1}(\tau\Delta\nu) \quad (2)$$

$$\tau = \tau_0 \exp \frac{E_a}{kT} \quad (3)$$

In which $\Delta\nu$ is the line width in Hz, $\delta\omega_0$ is the rigid line width in Hz, τ is correlation time in s, τ_0 is the correlation constant, E_a is the activation energy in Jmol^{-1}, k is the Boltzmann constant in JK^{-1} and T is temperature in K.

Attenuated total reflectance Fourier transform infrared spectroscopy (ATR-FTIR)

ATR-FTIR spectral data was acquired using an Alpha FTIR spectrometer (Bruker Optik GmbH, Ettlingen, Germany) equipped with a deuterated triglycine sulfate (DTGS) detector and a single-reflection diamond ATR sampling module

(Platinum ATR QuickSnap™) operating at a 45° angle of incidence. A background spectrum was individually acquired on a clean ATR surface prior to each sample measurement. A few milligrams of solid electrolyte sample was placed onto the 2×2 mm^2 sensing surface of the diamond ATR crystal before applying pressure to the top of the sample using an ergonomic clamp, and a few high-quality spectra were collected from each sample. The pressure applied by the clamp was estimated to be less than 20 MPa. The ATR-FTIR acquisition parameters used in the OPUS 6.0 software suite (Bruker) throughout the study included 4 cm^{-1} spectral resolution, 64 co-added scans, Blackman-Harris 3-Term apodization, Power-Spectrum phase correction, and a zero-filling factor of 2.

Positron annihilation lifetime spectroscopy (PALS)

PALS was performed to determine the free volume and relative number of free volume elements within the pure OIPC and PVDF nanofibre composite samples. The samples were assembled and run under dry nitrogen atmosphere at 20°C and 80°C. Two 1.5 mm thick sample disks were placed on either side of a ^{22}NaCl positron point source, which was enclosed in Mylar. The measurements were performed on an automated EG&G Ortec fast-fast coincidence system and a minimum of 5 files of 1×10^6 integrated counts with a timing resolution of 230 ns were collected. The spectra were de-convoluted using LT (version 9.0) software[34] to determine the average lifetime and intensity for each sample; the source correction was 1.703 ns and 3.798%. Each sample had three lifetimes and corresponding intensity components. The first lifetime was fixed to 0.125 ns and assigned to *para*-positronium formation; the second lifetime was ~0.4 ns and assigned to free positron annihilation within the sample; while the third component was associated with *ortho*-positronium (*o*-Ps) annihilation, and was used to measure the relative size and number of free volume elements in the samples. *o*-Ps is the bound state of a positron (e^+) and an electron (e^-) of the same spin. The *o*-Ps preferentially locates to areas of low electron density (i.e. free volume) and subsequently annihilates by colliding with another free electron from the sample. Therefore, the larger the free volume, the longer *o*-Ps lives, and hence the *o*-Ps lifetime (τ_3) can be used to estimate the radius of the free volume elements (r) via the Tao-Eldrup equation:

$$\tau_3 = \frac{1}{2}\left[1-\frac{r}{r+\Delta r}+\frac{1}{2\pi}\sin\left(\frac{2\pi r}{r+\Delta r}\right)\right]^{-1} \quad (4)$$

Where Δr is the empirical electron layer thickness (1.66Å)[35, 36]. The results are presented in supplementary information.

Results

Thermal behaviour

Figure 2 shows thermal traces obtained from DSC measurements on pure, 10 mol% lithium-doped [C_2mpyr][BF_4] and the corresponding PVDF nanofibre composites. The OIPC, [C_2mpyr][BF_4] undergoes several solid-solid phase transformations at low temperatures (labelled as IV to I in fig. 2) and stays in the solid-state plastic phase I over a broad temperature range from 64.5°C up to its decomposition temperature at around 250°C [26]. Mixing with lithium (the trace labelled as Y in fig. 2) introduces additional peaks at low temperatures below the phase IV to III transition and also after the transformation from phase II. The additional transitions were observed in other study and also reported for other Li mixtures of pyrrolidinium based OIPCs[26, 37]. Similar phase transitions were observed for the pure OIPC with incorporation of PVDF nanofibres (trace X'). Interestingly, the additional peak introduced by lithium-doping of the OIPC was not present in the lithium-doped PVDF composite sample (trace Y').

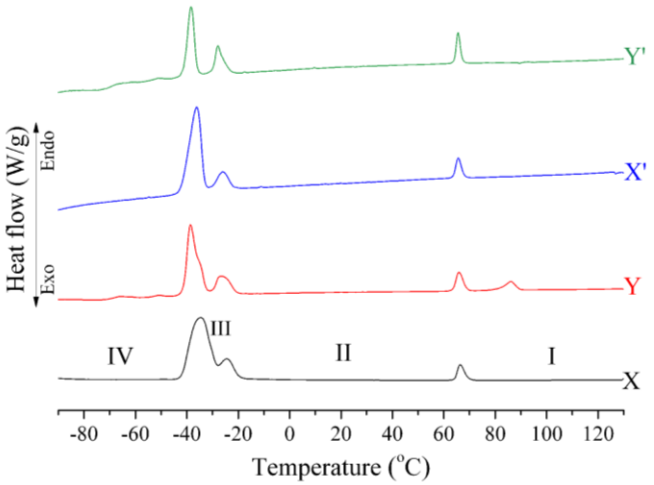

Figure 2. DSC thermal traces of pure [C_2mpyr][BF_4] (X), lithium-doped [C_2mpyr][BF_4] (Y), pure [C_2mpyr][BF_4]/PVDF composite (X') and lithium-doped [C_2mpyr][BF_4]/PVDF nanofibre composites(Y').

Ionic conductivity

Ionic conductivity of the materials as a function of temperature is illustrated in figure 3. The conductivity of the pure [C_2mpyr][BF_4] increases gradually in both crystalline phases with increasing temperature, revealing a jump around the phase II to I transformation temperature (fig. 3a). Lithium doping decreases the pure OIPC conductivity in phase II (fig. 3a). However, the conductivity of the lithium-doped [C_2mpyr][BF_4] significantly increases at the phase transformation and stays at much higher values; there is about 3 orders of magnitude difference in conductivity in phase I, compared to that of the pure OIPC. Similar behaviour was reported elsewhere for lithium-doped [C_2mpyr][BF_4] at higher lithium concentrations (above 8 mol%)[26].

The pure OIPC/PVDF nanofibre composite exhibits higher ionic conductivity than the neat OIPC in both crystalline phases over the whole measurement temperature range (fig. 3b). The conductivity of the pure OIPC composite is a smooth function of temperature, without a step at the phase transformation. The lithium-doped OIPC/PVDF composite (fig. 3c) exhibits

Journal Name RSCPublishing

ARTICLE

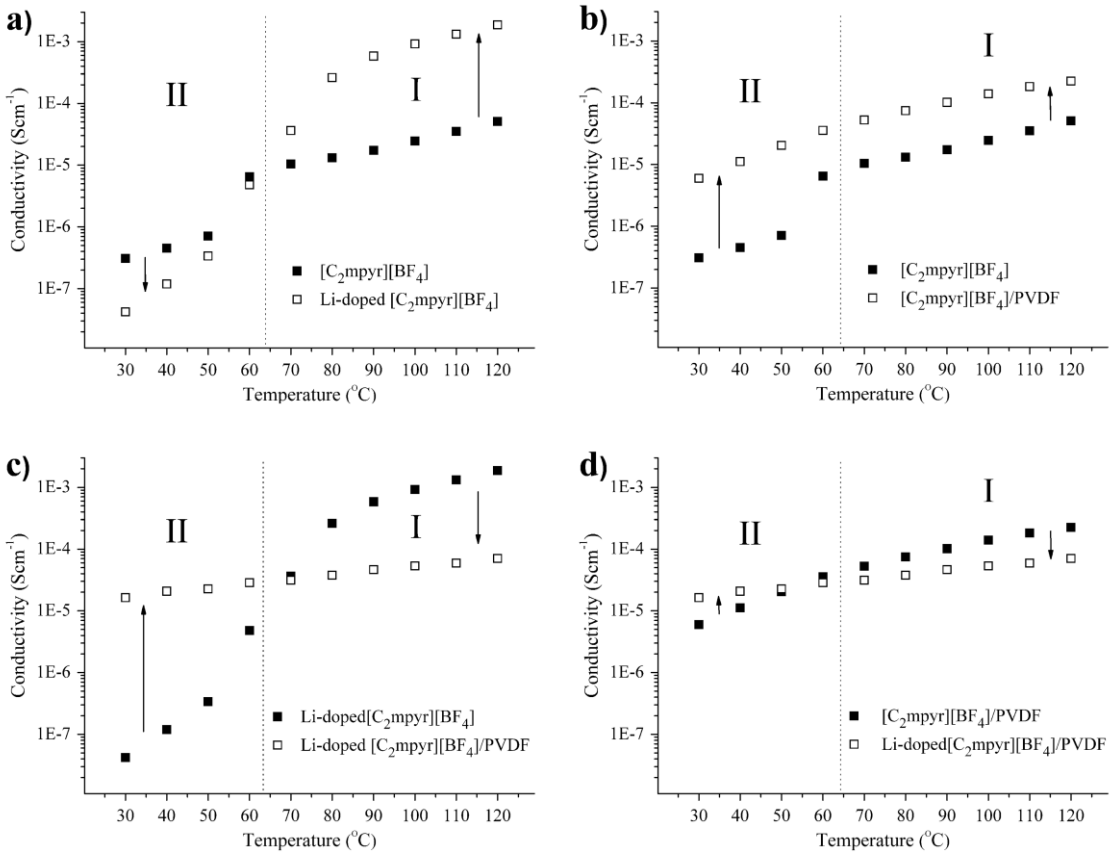

Figure 3. Ionic conductivities observed as a function of temperature: (a) pure [C_2mpyr][BF_4] and lithium-doped [C_2mpyr][BF_4]; (b) pure [C_2mpyr][BF_4] and PVDF composite; (c) lithium-doped [C_2mpyr][BF_4] and PVDF composite; (d) pure and lithium-doped PVDF composites.

remarkable high conductivity values in phase II compared to those of the fibre-free Li-doped OIPC (1.6×10^{-5} Scm^{-1} for Li-doped OIPC/PVDF composite versus 4.2×10^{-8} Scm^{-1} for the Li-doped OIPC at 30°C, about a 3 order of magnitude increase). However, the conductivity does not increase at the phase transition, and instead shows almost temperature independent behaviour. As a result, the conductivity of the Li-doped OIPC/PVDF composite is lower than that of the Li-doped material without fibres in phase I. Figure 3d compares the conductivity of composite materials in pure and lithium-doped states. Both materials exhibit an approximately linear increase in conductivity in both phases with increasing temperature, with different slopes, indicating different activation energies. The lithium-doped composite has higher conductivity values in phase II, but shows a smaller dependence on temperature compared to that of the pure OIPC composite; thus the lithium-doped composite has a lower conductivity in phase I than that of the pure OIPC composite.

The thermal activation energies for ion conduction calculated from the conductivity data in crystalline phase II and I of the materials are presented in table 1. The greatest change in the activation energy occurs upon lithium doping into the pure [C_2mpyr][BF_4] in phase II, which increases the activation energy from 34 kJmol^{-1} to 85 kJmol^{-1}. Interestingly, incorporation of fibres into the lithium-doped OIPC decreases the activation energy to be even less than that of the pure OIPC in phase II (from 85 kJmol^{-1} in Li-doped OIPC back to 13 kJmol^{-1} in the Li-doped PVDF composite). A similar trend is observed in phase I, although with smaller changes, compared to those in phase II. Interestingly, the activation energies in both crystalline phases of the ternary system containing both lithium salts and fibres within the OIPC are clearly lower than those of the binary systems of pure OIPC & fibres as well as combination of the OIPC & lithium salt, which is obvious from the gradients of the conductivity plots (figs. 3c & 3d).

Table 1. Activation energy of the materials in different crystalline phases

Material	Activation energy (kJmol^{-1}) ±1	
	Phase II	Phase I
[C_2mpyr][BF_4]	34	39
Li-doped [C_2mpyr][BF_4]	85	55
[C_2mpyr][BF_4]/PVDF	50	32
Li-doped [C_2mpyr][BF_4]/PVDF	13	17

NMR characterization

The ions $[C_2mpyr]^+$, $[BF_4]^-$ and Li^+ mobility in crystalline phases II and I of the pure and lithium-doped OIPC and the PVDF nanofibre composites were evaluated according to the probes acquired from ^1H, ^{19}F and ^7Li VT solid-state NMR measurements, respectively. The spectral line widths are indicative of the relative mobility of the corresponding ionic species. The results are presented in the following sections.

VT ^1H WIDE LINE SPECTRA

Figure 4 compares ^1H spectra of the pure and lithium-doped [C_2mpyr][BF_4] and the PVDF nanofibre composites at 20°C (phase II) and 80°C (phase I). The ^1H spectrum for the pure OIPC shows one component in the low temperature crystalline phase II (fig. 4a), but a small sharp narrow component is evident, superimposed on the broad signal in phase I, indicating the presence of some more mobile $[C_2mpyr]^+$ protons. Upon lithium doping, a small fraction of narrow component appears in phase II and grows significantly in phase I (at 80°C) (fig. 4a). This indicates that a substantial fraction of the pyrrolidinium cations gain a higher degree of mobility upon addition of 10 mol% $LiBF_4$ in phase I. In contrast, a slight increase in the linewidth was observed in phase II. The line width of the broad components was almost the same in phase I, while the narrow component in phase I is broader for the 10 mol% $LiBF_4$ doped sample.

In the presence of fibres (fig. 4b), the narrow component appeared at lower temperatures, where the pure OIPC was in phase II. This indicates that some cations are becoming mobile more readily when fibres are incorporated into the system. The narrow component seems to have a greater integral compared to that in the pure OIPC spectrum in phase I, indicating an increase in the population of the mobile species in the system. However, both narrow and broad components are broadened in both phases, indicating that fibres limit the increase in cation mobility in the pure system.

The composite behaviour is quite different in the presence of lithium ions (figs. 4c & 4d). In phase II, the linewidth is significantly broadened, which suggests an increase in the rigidity of the OIPC cation. Phase I also shows an increase in linewidth of the narrow component when fibres are incorporated into the Li-doped OIPC. Thus, it appears that overall the $[C_2mpyr]^+$ cations have decreased mobility in the composite containing $LiBF_4$, especially in phase II.

Figure 5 presents the integral analysis of the narrow component of the ^1H spectra as a function of temperature. These data clearly show the effects of lithium doping and addition of PVDF fibres on the fraction of mobile cations (i.e. the narrow component). The most dramatic effect is observed upon addition of Li to the OIPC in phase I, consistent with the increase in conductivity (figs. 5a & 3a). In the pure OIPC, the fibres increase the fraction of mobile component (fig. 5b), whereas, when Li is present, the mobile fraction is decreased in phase I and very slightly increased in phase II (fig. 5c), interestingly consistent with the trend observed in conductivity data (fig. 3c).

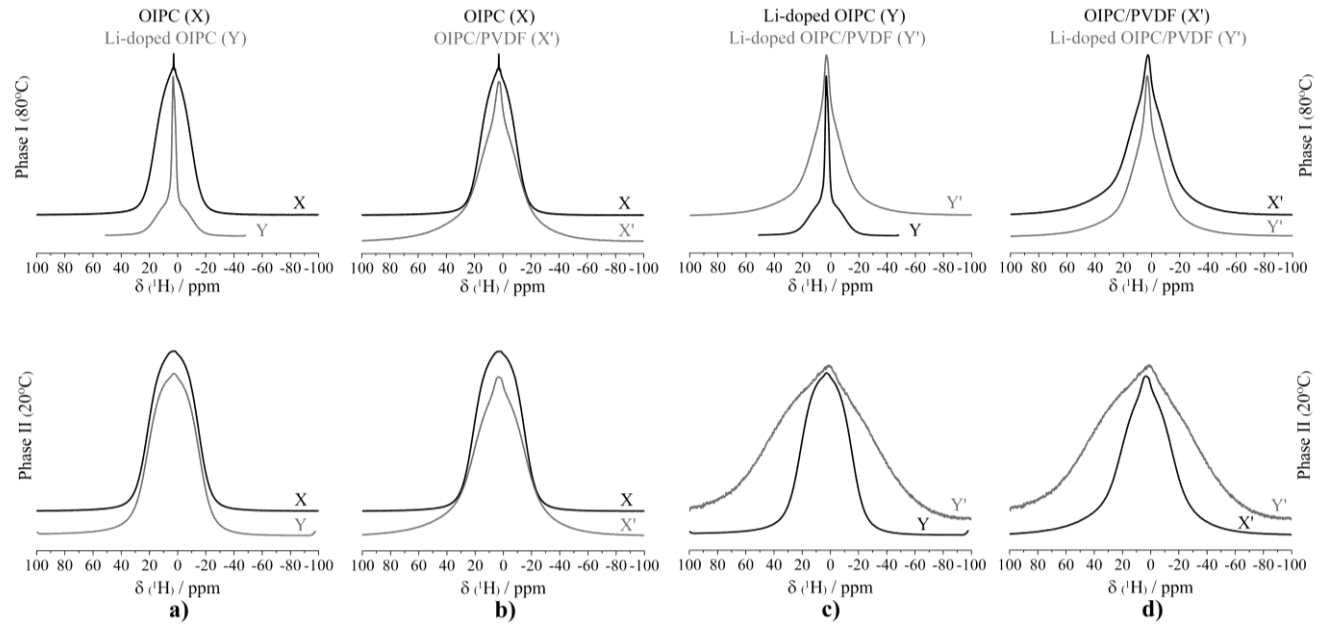

Figure 4. ^1H spectra for crystalline phase II (20°C) and phase I (80°C) of: (a) pure and lithium-doped [C_2mpyr][BF_4] (X,Y); (b) pure [C_2mpyr][BF_4] and composite (X,X'); (c) lithium-doped [C_2mpyr][BF_4] and PVDF composite (Y,Y'); (d) pure and lithium-doped PVDF composites (X',Y').

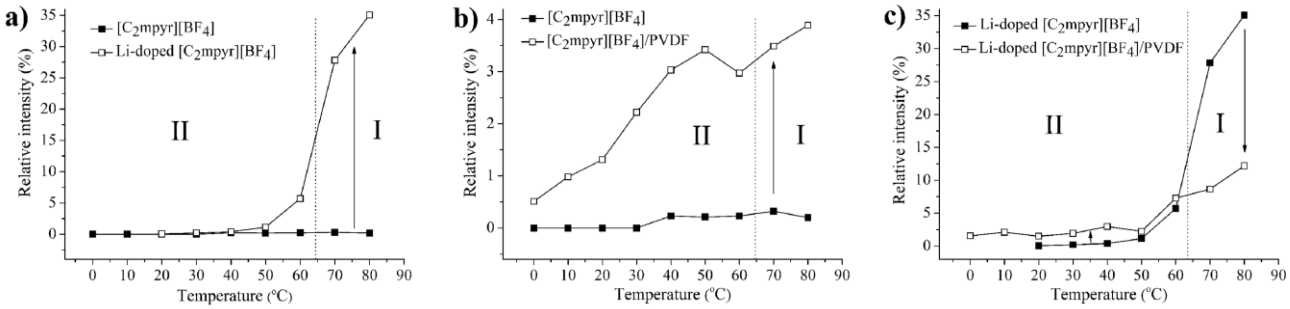

Figure 5. Relative intensity of the narrow component in ^{1}H spectra as a function of temperature for (a) pure OIPC and lithium-doped OIPC; (b) pure OIPC and PVDF composite; and (c) lithium-doped OIPC and lithium-doped composite, representing the percentage of the narrow component of the fitted ^{1}H signal relative to the total spectrum.

VT-SOLID-STATE ^{19}F SPECTRA

Figure 6 compares ^{19}F spectra for pure and lithium-doped $[C_2mpyr][BF_4]$ and their composites in different crystalline phases II (20°C) and I (80°C). A significant decrease in the linewidth of the spectrum for the pure OIPC is observed at the phase II to I transformation (fig. 6a). A slight increase in line width of the spectrum in phase II for the pure OIPC is observed upon lithium doping (fig. 6a). An additional signal arises in the presence of lithium in phase I, suggesting that two separate $[BF_4]^-$ containing phases coexist at this temperature. Broadening in the linewidth in both crystalline phases is observed for the pure material when it is introduced within the PVDF nanofibre network (fig. 6b). Interestingly, the lithium-doped OIPC exhibits again different behaviour compared to that of the pure material in phase II in the presence of PVDF nanofibres by exhibiting narrowing (fig. 6c). Surprisingly, the additional signal that was previously observed in the lithium-doped OIPC in phase I disappeared after incorporating within the PVDF fibres. This observation suggests the fibres homogenize the environment within the lithium-doped OIPC by changing two different $[BF_4]^-$ containing phases into a single one.

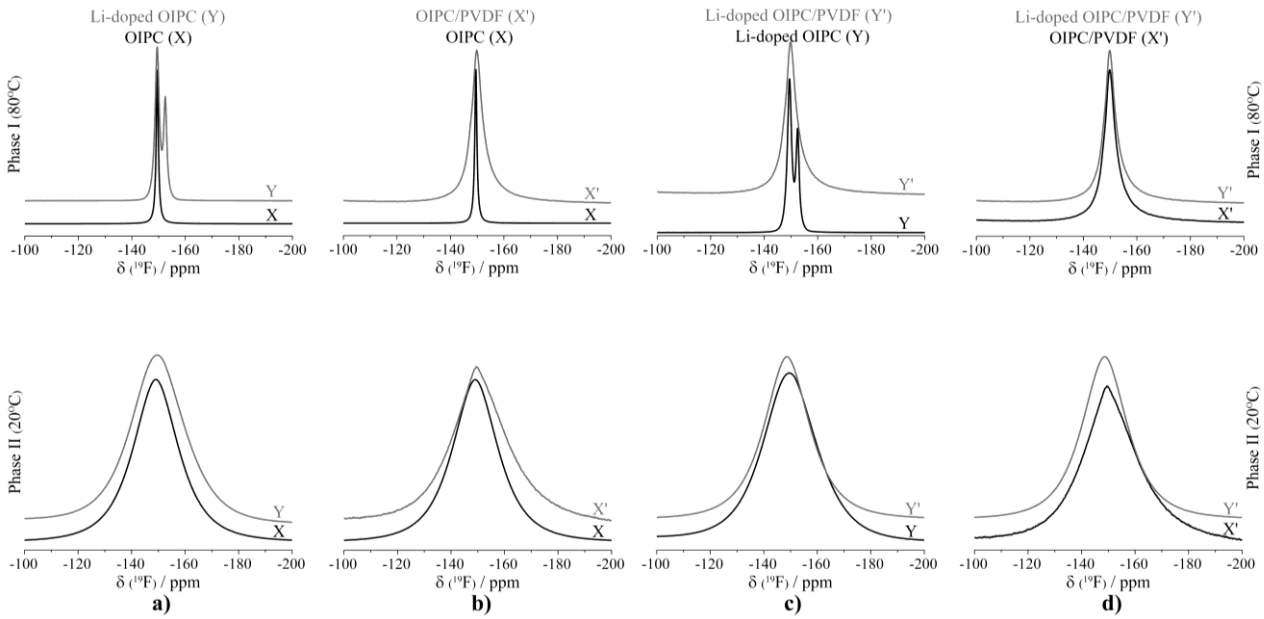

Figure 6. ^{19}F spectra for crystalline phase II (20°C) and phase I (80°C) of : (a) pure and lithium-doped $[C_2mpyr][BF_4]$ (X,Y); (b) pure $[C_2mpyr][BF_4]$ and PVDF composite (X,X'); (c) lithium-doped $[C_2mpyr][BF_4]$ and composite (Y,Y'); (d) pure and lithium-doped PVDF composites (X',Y').

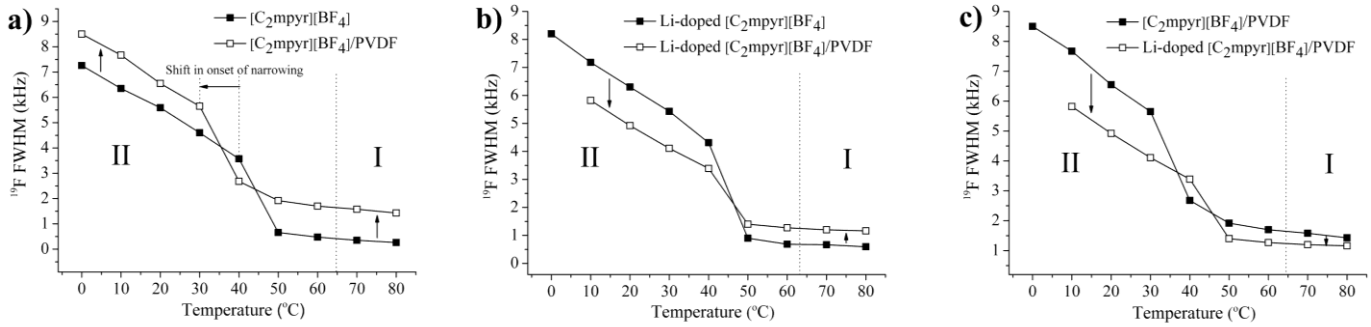

Figure 7. ^{19}F peak width change with temperature observed for: (a) pure OIPC and pure composite; (b) Lithium-doped OIPC and the PVDF composite; (c) pure and lithium-doped composites.

Figure 7 presents ^{19}F line widths for the pure and lithium-doped systems. The change in the start of the narrowing of the spectra (about 10°C shift to lower temperatures in pure OIPC) suggests that the incorporation of fibres facilitates phase I anion fast dynamics at lower temperatures while the pure OIPC still has phase II rigid anion dynamics (fig. 7a). However, the anion becomes less mobile in both phases according to broadening of the ^{19}F NMR spectra in the composite. The lithium-doped spectrum exhibits narrower line widths over the whole temperature range of phase II in the presence of fibres, but shows broadening in phase I (fig. 7b). The composite materials in pure and lithium-doped states exhibit less difference in phase I while in phase II the lithium-doped composite has more narrow ^{19}F spectrum compared to that of the pure composite (fig. 7c). This suggests greater mobility of the $[BF_4]^-$ anion in the composite material in the presence of lithium.

VT-Solid-state ^{7}Li spectra

Figure 8 shows ^{7}Li spectra for the lithium-doped $[C_2mpyr][BF_4]$ and it's composite. The spectrum exhibits a broad signal at lower temperatures (0°C–50°C) for the lithium-doped OIPC, suggesting that Li ions are not particularly mobile in phase II (fig. 8a). A narrow component appears at around 50°C, and gradually replaces the broad component as temperature is increased to the phase transition temperature of 63°C. The spectrum is even broader at 0°C when the material is cast within the fibres (fig. 8b). However, the spectrum narrows significantly in phase II over a broad temperature range from 20°C up to the phase transition temperature (fig. 8c). Furthermore, the narrow component initiates at much lower temperatures than for the neat lithium-doped OIPC (i.e. without fibres). More importantly, the composite exhibits a remarkably shorter correlation time in phase II for the lithium ion than in the neat lithium-doped OIPC (fig. 8d). This suggests that the lithium ion stays for a shorter duration at each hopping site in phase II in presence of fibres. However, both materials start to exhibit similar correlation times for the lithium ion in phase I. In addition, the extracted activation energy value for the Li-doped composite is smaller compared with the neat Li-doped OIPC (50.2 $kJmol^{-1}$ for the composite compared to 53.7 $kJmol^{-1}$ for the Li-doped OIPC, uncertainty ±0.001).

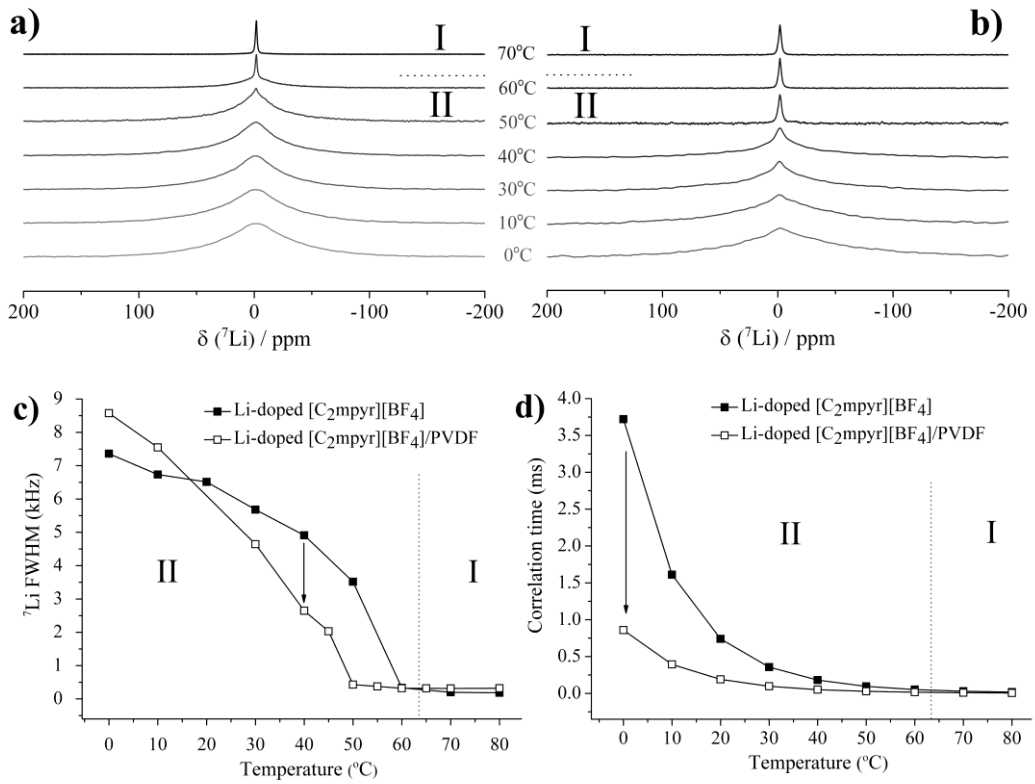

Figure 8. VT-static ^{7}Li spectra of (a) Li-doped OIPC and (b) Li-doped OIPC/PVDF composite; (c) ^{7}Li line width as a function of temperature; and (d) Li-ion correlation time as a function of temperature.

ATR-FTIR spectroscopy

Figure 9 shows room temperature IR spectra acquired for the pure and lithium-doped [C_2mpyr][BF_4], and the PVDF composites. The combination of the OIPC and PVDF fibres, as well as the effects of the Li doping, led to several changes in the spectral features, particularly shifts of the bands corresponding to [C_2mpyr][BF_4] and/or PVDF fibres, which are summarized in Table 2.

The spectrum of the Li-doped OIPC indicates no significant influence of the Li-doping on the alkyl and BF_4 structures showing only a slight shift in one of the BF_4 stretching modes, to 770 cm^{-1}. Instead, the doped Li atoms formed a strong interaction with the pyrrolidinium ring, as clearly evidenced through the presence of a new ring mode corresponding to the shoulder band at 977 cm^{-1} (arrowed in fig. 9), which was observed in association with shifts of the existing ring modes to higher wavenumber values at 1047 and 1029 cm^{-1}. The intensity of the ring breathing mode at 1029 cm^{-1} also appeared to be noticeably reduced in the Li-doped OIPC, further emphasizing the direct interaction of the added Li ions on the pyrrolidinium ring that led to a change of the ring orientation. These changes may be a result of packing within the crystalline structure of the solid material and electrostatic repulsion between the Li^{+} and [C_2mpyr]$^{+}$ cations having the effect of forcing the pyrrolidinium ring to adopt a new conformation at a higher energy level.

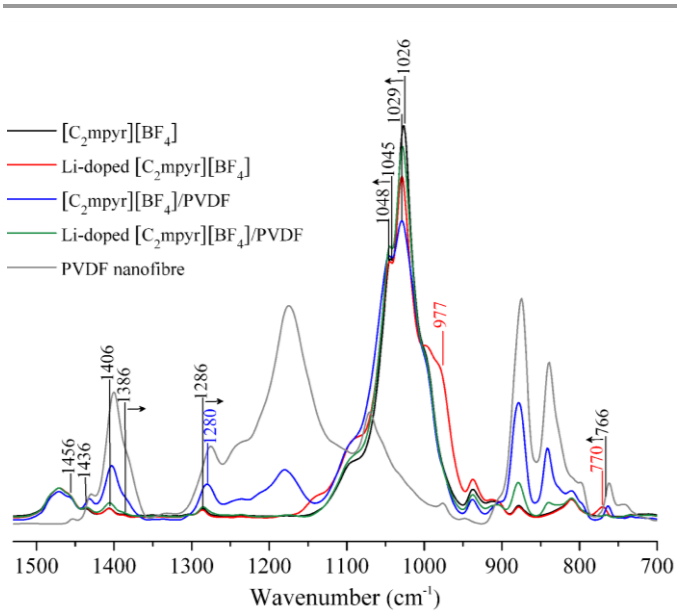

Figure 9. ATR-FTIR spectra of the pure [C_2mpyr][BF_4], PVDF nanofibre composite, Li-doped [C_2mpyr][BF_4], Li-doped PVDF composite and PVDF nanofibre at room temperature.

Table 2. Wavenumber values and assignments of the ATR-FTIR bands observed in the Li-doped $[C_2mpyr][BF_4]$ and PVDF composites in comparison to those found in the reference spectra of the$[C_2mpyr][BF_4]$ and the PVDF fibres.

Related structure	Observed wavenumber values[a] (cm^{-1})					Band assignment[b]	Ref.
	$[C_2mpyr][BF_4]$	PVDF	$[C_2mpyr][BF_4]$ /PVDF	Li-doped $[C_2mpyr][BF_4]$	Li-doped $[C_2mpyr][BF_4]$ /PVDF		
BF_4[c]	1286 995 766		1280(↓) 995(–) 763(↓)	1286 (–) 995 (–) 770(↑)	1286 (–) 995 (–) 766 (–)	ν(BF) ν(BF) $\nu_s(BF_4)$	38, 39
Pyrrolidinium ring	1045 1026		1048 (↑) 1029 (↑)	1048 (↑) 1029 (↑) 977	1048 (↑) 1029 (↑)	δ(ring) Ring breathing, ν(Et-N), ν(Me-N) Ring mode	39-42
Alkyl	1484 1471 1456 1436 1406 1386 1098 938 810		1484 (–) 1471 (–) 1455 (↓) 1432 (↓) 1403 (↓) 1382 (↓) 1101 (↑) 938 (–) 810 (–)	1484 (–) 1471 (–) 1456 (–) 1436 (–) 1406 (–) 1386 (–) 1098 (–) 938 (–) 810 (–)	1484 (–) 1471 (–) 1456 (–) 1436 (–) 1406 (–) 1386 (–) 1100 (↑) 938 (–) 810 (–)	$\delta(CH_2)$ (ring) $\delta_{as}(CH_3)_{Me}$ $\delta(CH_2)$ $\delta_s(CH_3)$ $\delta_s(CH_3)_{Et} + \delta_{wag}(CH_2)$ $\nu_{as}(C-N) + \delta_s(CH_3)_{Et}$ $\delta_{rock}(CH_3) + \delta_{rock}(C-H)$ $\nu(C-C)_{Et}$ γ(CH)	39, 41, 42
PVDF		1175 839	1181 (↑) 842 (↑)		1175 (–) 839(–)	δ(C–F) $\gamma(CH_2)$	42

[a] Direction of the band shift with respect to the position of the corresponding bands found in the reference spectrum of the pure $[C_2mpyr][BF_4]$ or the pure PVDF fibres: (–) = no shift; (↑) or (↓) = shift to a higher or a lower wavenumber value, respectively.

[b] Symbols used to represent vibrational modes: ν_{as} = asymmetric stretch; ν_s = symmetric stretch; δ_{as} = asymmetric deformation (bend); δ_s = symmetric deformation (bend); γ = out-of-plane deformation; Et = ethyl ($-C_2H_5$); Me = methyl ($-CH_3$).

[c]The modes at 766, 995 and 1286 cm^{-1} are not fundamentally IR active. However, the 766 cm^{-1} mode has been shown to be not totally inactive (Katsyuba et al.[39]) when the $[BF_4]^-$ was paired to $[EMIM]^+$ (i.e., *cf* $[C_2mpyr]^+$) which was attributed to breaking of the inversion symmetry associated with the anion, whilst bands at 995 and 1286 cm^{-1} were shown to be principle funadamental modes attributed to ν(BF(5)) and ν(BF(4)) + ν(BF(2)) respectively. The expected band ν(BF(3)) stretching mode at 1070 cm^{-1} was not reported due to difficulty in fitting caused by overlapping with strong $[C_2mpyr]^+$ ring and alkyl bands.

The incorporation of the pure OIPC into the nanofibre matrix of PVDF caused shifts of the bands that represent $[BF_4]^-$ vibrations (i.e. 1286 and 765 cm^{-1}) and most of the alkyl-related modes (i.e. 1456, 1436, 1406 and 1386 cm^{-1}) to lower wavenumber values, while the characteristic bands attributable to pyrrolidinium ring vibrations (i.e. 1045, 1026 and 879 cm^{-1}) and the PVDF moiety (i.e. 1175 and 839 cm^{-1}) were oppositely shifted to higher wavenumber values. Such contrast in features suggests that the new interactions formed between $[C_2mpyr][BF_4]$ and PVDF, which affected the overall molecular orientation of the composites in a way which stabilized the BF_4 and alkyl bonding interactions within the $[C_2mpyr][BF_4]$ structure into a lower energy form, but destabilized the conformation of the pyrrolidinium ring and the PVDF polymeric chains. The substantial decrease in intensity of the ring breathing mode at 1029 cm^{-1} observed in the spectrum of the $[C_2mpyr][BF_4]$/PVDF composites further indicates that the new conformation likely created a structural hindrance that constrained the breathing vibrational mode of the pyrrolidinium ring

Upon incorporating the Li-doped OIPC into the PVDF matrix, the BF_4 vibrations, as well as most of the alkyl-related modes, remain unchanged. Only the C-H rocking deformation modes were shown to be slightly shifted to a higher wavenumber value. As mentioned previously, without Li-doping, the BF_4 stretching vibrations and most of the alkyl modes were shown to be shifted after being combined with the PVDF fibres. Therefore, the presence of the added Li ions in the composite matrix likely stabilized the $[BF_4]^-$ anions as well as the conformation of the alkyl groups, making them insensitive (inert) to the subsequent combination into the PVDF matrix. More interestingly, the new ring mode that was previously observed at 977 cm^{-1} in the Li-doped OIPC disappeared after combining with the PVDF nanofibres; instead, the bands in this range appear similar to those of the $[C_2mpyr][BF_4]$/PVDF composite spectrum. This observation suggests that the PVDF has a strong influence on the orientation of the pyrrolidinium ring in Li-doped OIPC, maintaining the orientation of the ring to be similar to that found in the pure OIPC.

Crystallography

Figure 10 presents synchrotron X-ray diffraction patterns for the pure and lithium-doped $[C_2mpyr][BF_4]$ and for the pure and lithium-doped PVDF nanofibre composites at different crystalline phases IV, II and I, which were acquired at -80°C, 50°C and 100°C, respectively.

Changes in the diffraction patterns of the pure OIPC with an increase in temperature indicate ion species orientation in different crystalline structures in each phase. The decreasing number of peaks demonstrates an increase in crystal symmetry with increasing temperature (see fig. S1 in supplementary information). The lattice system changes from monoclinic to trigonal through phase transformation IV to II and to cubic system in phase I (table. 3). Given an assumed density in the order of ~1.2 gcm^{-3} [28-30] in phase II, it was calculated that each unit cell contains two ion pairs for the lower temperature phases, and four ion pairs in the high-temperature phase. On this basis, the increase in percentage volume change associated with an ion pair in the unit cell is 11.4% for phase IV to II transitions while the phase II to I transition results in a further volume increase of 4.6% (equivalent to a decrease in theoretical density of 9.7% (IV to II) and 5.0% (II to I), respectively). The values are consistent with the scaled changes in enthalpy of transitions observed in the DSC traces and also with the related entropy values which is greater for phase IV to II transition (52.7 $JK^{-1}mol^{-1}$) compared to the phase II to I transition (4.3 $JK^{-1}mol^{-1}$) [25]. This reflects the gradual development of orientational and/or rotational disorder through the transitions into the most plastic phase I, which gives rise to fewer reflections in the diffractogram owing to higher symmetry in the crystal structure. As a result, the dimensions of the unit cell increase to accommodate 4 ion pairs in contrast to the 2 ion pairs found in unit cells of the lower temperature phases[43].

Lithium doping of $[C_2mpyr][BF_4]$ introduces significant changes in the transformation sequence (the red traces in the accompanying figures, labelled as Y). While the structure is the same as that of the pure material in phases IV (monoclinic) and I (cubic), a monoclinic structure is found in phase II. The unit cell volume is also considerably increased in the low temperature phase IV (801.9% increase in the cell volume , equivalent to 15.7% decrease in the theoretical density) and in phase II (755.6% increase in volume, equivalent to 11.6% decrease in theoretical density), reflecting increased number of ion pairs to create the unit cell (i.e. to accommodate 16 ion pairs compared with 2 in the pure system) but, interestingly, the unit cell volumes and theoretical density values were very close for both Li-doped and pure systems in phase I, with both showing cubic structures with 4 ion pairs per unit cell. Additional peaks are also present at low temperatures from a minor high symmetry phase in the lithium-doped OIPC. Interestingly, the change in volume associated with an ion pair in phase IV to II transition is less than for the pure material (5.5% in Li-doped OIPC compared to 11.3% in the pure OIPC). This appears to be due to the role of lithium in maintaining the structure in a monoclinic system. Interestingly, consistent with the removal of additional transition in the DSC trace at 86°C, the minor phase also disappears from the XRD patterns which were collected at 100°C (above that transition) and as a result a decrease in the cell volume per ion pair is observed in the Li-doped OIPC, which is not the case in the other materials.

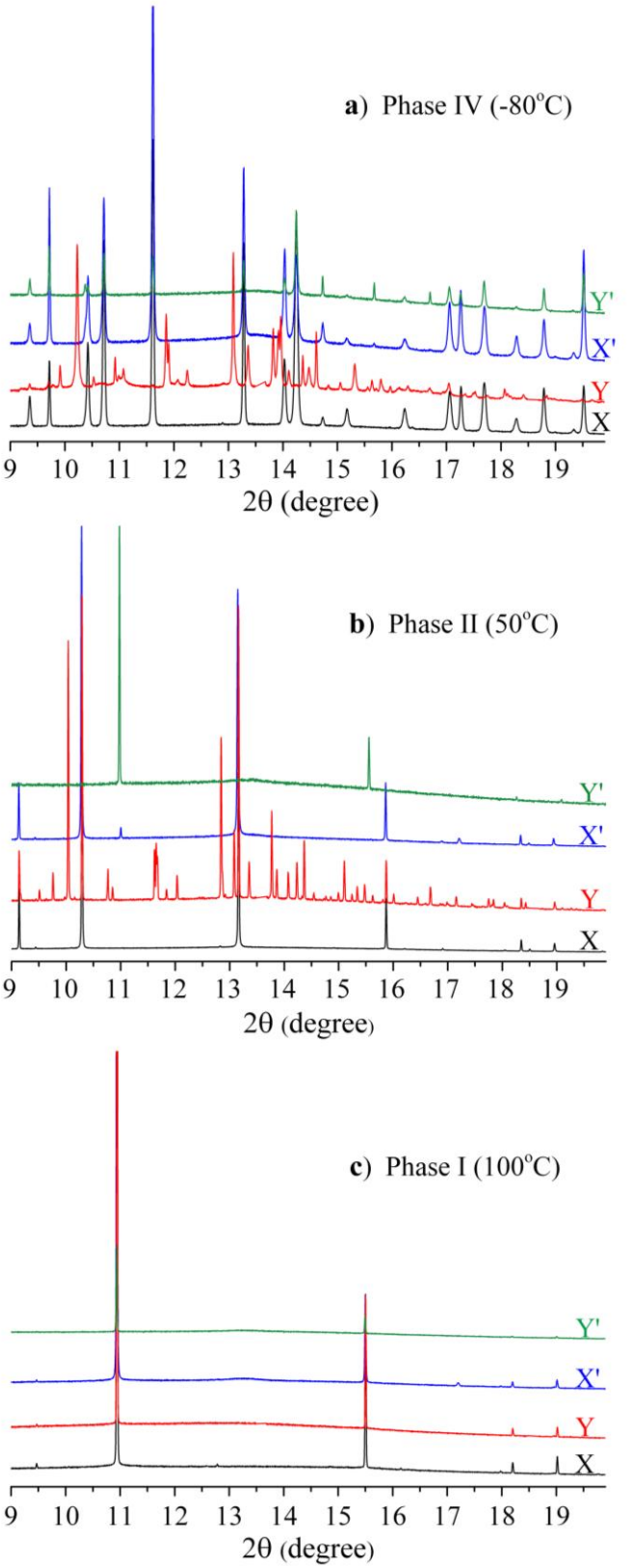

Figure 10. Synchrotron X-ray diffraction patterns for pure $[C_2mpyr][BF_4]$ (X), Li-doped $[C_2mpyr][BF_4]$ (Y), pure $[C_2mpyr][BF_4]$/PVDF composite (X') and Li-doped PVDF composite (Y') at different crystalline phases: (a) phase IV, -80°C; (b) phase II, 50°C; (c) phase I, 100°C.

Journal Name RSCPublishing

ARTICLE

Table 3.Crystallographic parameters of the materials

Material	T (°C)	phase	Lattice system	Space group	a	b	c	α	β	γ	$V_{unit\ cell}$ (Å^3)	Z	$V_{ion\ pair}$ (Å^3)	ρ (g cm^{-3})
[C_2mpyr][BF_4]	-80	IV	monoclinic	P21 (4)	7.3542(1)	11.0153(2)	6.4457(1)	90	107.9431(9)	90	496.764(12)	2	248.382(6)	1.34
	50	II	trigonal	P31c (159)	7.2495(1)	-	12.1518(1)	90	90	120	553.076(8)	2	276.538(4)	1.21
	100	I	cubic	Fm-3m (225)	10.4959(1)	-	-	90	90	90	1156.26(2)	4	289.065(5)	1.15
[C_2mpyr][BF_4]/PVDF	-80	IV	monoclinic	P21 (4)	7.3548(2)	11.0134(3)	6.4457(2)	90	107.934(1)	90	496.744(27)	2	248.372(14)	1.34
	50	II	trigonal	P31c (159)	7.2540(1)	-	12.1683(2)	90	90	120	554.519(13)	2	277.259(7)	1.20
	100	I	cubic	Fm-3m (225)	10.4966(1)	-	-	90	90	90	1156.501(18)	4	289.125(5)	1.15
Lithium-doped [C_2mpyr][BF_4]	-80	IV	monoclinic	C2 (5)	21.9453(7)	16.0118(3)	12.8294(4)	90	83.668(2)	90	4480.54(21)	16	280.034(13)	1.13
	50	II	monoclinic	C2 (5)	22.4471(9)	16.3360(8)	12.9879(9)	90	83.543(4)	90	4732.40(43)	16	295.775(27)	1.07
	100	I	cubic	Fm-3m (225)	10.4936(1)	-	-	90	90	90	1155.509(27)	4	288.877(7)	1.09

Z: ion pair per unit cell

Pure [C_2mpyr][BF_4], within the PVDF nanofibre network exhibits similar patterns to those of the pure plastic crystal, with the same diffraction peaks observed for all crystalline phases (the blue traces in the accompanying figures, labelled as X'). This suggests the same lattice systems are present in the composite as in the pure OIPC for all crystalline phases. However, some changes at each crystalline phase were observed. Figure 11 shows the response of the pure OIPC structure to the introduction of the PVDF fibres in different phases. The patterns indicate shifts in peak position in the high temperature phases II and I; this is not observed in the low symmetry phase IV. The shift in peak position towards smaller diffraction angles indicates an expansion of the lattice parameters in phases II and I with the addition of fibres as shown in table 3. The effect is pronounced in phase II with exhibiting the greatest volume change of the unit cell by fibres addition, which is also reflected in theoretical density change. This is while, change in peak width as well as peak intensity is observed in all phases. However, the effect is different in phase IV compared to phases II and I. The intensity response of the system to fibre incorporation is heterogeneous in the monoclinic phase IV (peaks labelled as B in fig.11) while a more homogenous response is seen in phases II and I (peaks labelled as A in fig.11). This suggests the existence of orientation or texture in the low temperature structure, with low symmetry which disappears with the increase in symmetry at higher temperatures (in phases II and I).

The broader peak widths are indicative[44] of smaller crystallite sizes or higher lattice strains when the PVDF nanofibres network is present. This is consistent with the DSC data which exhibit a decrease in the entropy of transitions with fibres incorporation, suggesting formation of a disordered or amorphous phase in the structure in the presence of fibres, probably in the interface areas [25].

Interestingly, the lithium-doped composite exhibits very similar patterns to those of the pure [C_2mpyr][BF_4] and the pure composite.

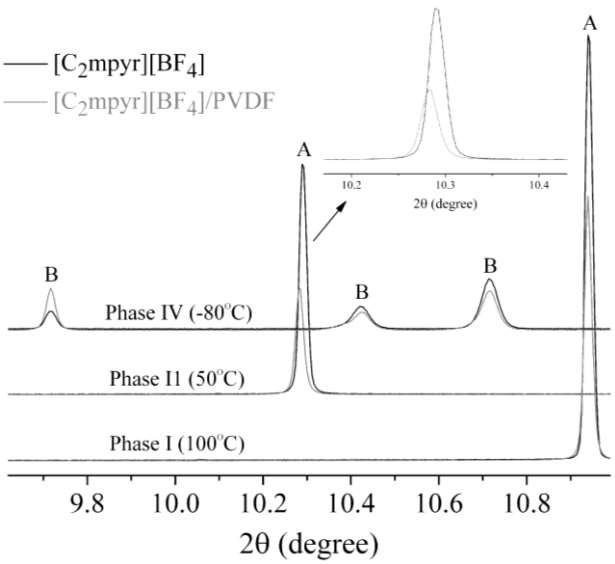

Figure 11. XRD patterns indicating the effect of fibre addition to pure [C_2mpyr][BF_4] in phases IV (-80°C), II (50°C) and I (100°C).

Discussion

Structure and dynamics in pure $[C_2mpyr][BF_4]$

As previously reported, we observe multiple phase transitions in the pure material with varying changes in entropy of the transitions, suggesting different degrees of local disorder brought about by changes in conformational/orientational and/or rotational modes of the ionic species in the material throughout the transformations. The transitions lead to a re-orientation of the structure towards increased symmetry, as observed by XRD, with increasing temperature. A higher-symmetry diffraction pattern has previously been observed in pure OIPCs, and has been related to the presence of rotatory phases and higher local dynamics with isotropic tumbling of the molecular or ionic species on lattice sites[38, 43]. A detailed investigation based on quantum chemical calculations and advanced solid-state NMR studies indicates that various ion dynamics occur in different crystalline phases for the pure OIPC under investigation here [45, 46]. Relatively rigid, frozen cation dynamics, with a restricted puckering fluctuation of the alkyl group around the pyrrolidinium ring, was suggested in phase IV. A significant increase in the cation dynamics was observed at the phase IV to III transition, but these motions are still not enough to observe full exchange between carbon sites in the pyrrolidinium ring. Complete rotation of the ring, around a single axis, was only observed in phase II. Full isotropic rotation of the cation is established after the phase transformation from II to I. The $[BF_4]^-$ anion, on the other hand generally exhibits tumbling motion with dynamics coupled to those of the cation. Significant narrowing of the ^1H and ^{19}F spectra at the II to I phase transition, as described above (Figs. 4-7), indicates an increasing degree of mobility for both ionic species. In particular, the ^{19}F narrowing to liquid like linewidths suggests translational motion of the $[BF_4]^-$ anion, which most likely dominates the increase in ionic conductivity. A small but distinct narrow component also becomes observable at the higher temperature phase transition in the ^1H spectrum. This indicates the activation of isotropic fast rotational, and likely translational, motion of the cation in phase I from its monoaxial motion in phase II; this will also contribute a small number of cation charge carriers to the conductivity. These changes in the ion dynamics seen via NMR result in the observed jump in the ionic conduction of the material at the transformation from phase II to I (fig. 3a). Therefore, we clearly see that moving towards a more symmetric OIPC structure results in high conductivity by activating more dynamic modes of either ionic species; in this case the $[BF_4]^-$ ion seems to dominate conduction (Fig. 6a).

Lithium salt addition

Lithium doping introduces completely different crystallographic behaviour in phases IV to II, with only phase I exhibiting the same diffraction pattern. At low temperatures, a secondary phase with high symmetry is observed in addition to the matrix phase, according to diffraction pattern analysis. This is consistent with the presence of the new ring mode bands observed in the ATR-FTIR spectra of the lithium-doped OIPC at room temperature. Furthermore, the DSC shows additional transitions at low temperatures below the IV to III transformation, which suggests that the distinct new phase nucleates at lower temperatures. This new phase, unlike the pure OIPC material, does not allow the matrix phase transition from monoclinic to trigonal between -80 and 50°C, instead maintaining a monoclinic phase in phase II. The NMR data clearly show that the $[BF_4]^-$ anion exists in two environments, most likely because of the presence of the second phase, which we also observe in the DSC, ATR-FTIR and XRD data. Interestingly, the conductivity in phase II is significantly lower in the case of the Li-doped systems; The phase behaviour discussed above, appears to hinder both cation and anion mobility in phase II, according to the slight increase in ^1H and ^{19}F line widths upon lithium doping. We note, however, that another possible cause for this lower conductivity could be the formation of a second phase at grain boundaries, which present a lower energy barrier for nucleation and growth of this second phase[47]. The precipitation of a second phase at grain boundaries can block pathways for ion diffusion through the boundaries, which can then act as another restriction or barrier to ion transport in the system[14, 48]. The formation of this second phase also means that a portion of Li ions in phase II may be unavailable to transport charge through the bulk and/or grain boundaries. The decrease in ionic conductivity of phase II above a certain lithium concentration was observed elsewhere, which did not have further investigation[26]. The additional peak in the DSC thermogram just above the phase II to I transition for the lithium-doped OIPC suggests a gradual dissolution of this new phase into a cubic structure observed in phase I of the pure OIPC (fig. 2). The similar diffraction patterns for pure and lithium-doped OIPC at 100°C (in phase I) indicate the same cubic lattice system and space group for the lithium-doped and pure OIPC, supporting the idea of complete dissolution of the second phase upon moving towards higher temperatures in phase I. This would lead to a solid solution in the cubic structure with increased lithium ion concentration (fig. 10, table. 3). As a result of the dissolution of this second phase upon increasing temperature towards phase I, increased dynamics (and probably diffusion) are observed in the ^1H spectrum, indicating activation of significant numbers of pyrrolidinium cations with higher mobility (fig. 4a). The population of these mobile sites grows significantly with increasing temperature in phase I (fig. 5a). The release of a portion of lithium ions as a result of dissolution of the second phase into the structure introduces additional charge carriers into the system. An additional effect of this dissolution may be to remove second phase precipitates from the grain boundaries, allowing grain boundary diffusion in the lithium doped system. All of these effects result in facilitating ion transport in the system and thus a significant increase in ionic conductivity is observed in phase I after lithium doping (fig. 3a).

Pure [C_2mpyr][BF_4] incorporation within PVDF nanofibres

Whilst the pure OIPC retains its crystalline structure in all phases when cast within PVDF fibres, the lattice parameters are nevertheless altered. The fibres slightly expand the lattice parameters, particularly in phase II, leading to greater free volume for rotational motions (and possibly diffusion) of the ions. This is also reflected in the NMR spectra as follows. Introduction of the fibres initiates the mobile component in the ^{1}H spectra at much lower temperatures when the OIPC is still in phase II (fig. 4b). Furthermore, the population of these mobile cation sites increases in the presence of fibres and continues to increase further with increasing temperature towards phase I (fig. 5b). Addition of fibres also facilitates the onset of anion dynamics at lower temperatures (fig. 7a). These effects result in the observed higher ionic conduction in both phases II and I of the composite material compared with the pure OIPC. However, the presence of fibres suppresses (or imposes an upper limit on) the magnitude of the ion dynamics (in both 'mobile/narrow' and 'static/broad' segments of the ^{1}H spectra) as observed by the broadening of both the ^{1}H and ^{19}F spectra, despite the increased fraction of 'mobile' cations. In the case of the anion, there is only one resonance and this broadens in the composite, also suggesting decreased anion mobility. As a result, the temperature dependence of the conductivity in the composite does not show a step change at the phase transition. To summarize, cation dynamics play the major role in improving conduction in both phase II and phase I of this composite system based on pure [C_2mpyr][BF_4]. Preliminary results from PALS measurements on the pure materials help to understand the cation dynamic behaviour in this composite system. The PALS results indicate an increase in average free volume size within the pure OIPC upon addition of fibres (as evidenced by the larger tau3 seen in fig. S5). The free volume sites (previously associated with vacancies[49]) expand in going from phase II (at 20°C) to phase I (at 80°C). The existence of structural defects, such as vacancies, was previously found to promote rotational and translational motions within OIPCs, which facilitate ion transport through their structure. The close relationship between the size/number of defects and ionic conduction in few studies confirms the critical role of defects in ionic conductivity behaviour of the OIPCs [49, 50]. Baugham and Turnbull also reported rotational motion of the species is less hindered in the vicinity of vacancies[51]. Therefore, the increased size of free volume sites in the composite correlates with the increase in the population of mobile cations observed in the NMR and hence higher conductivity.

An additional effect of the fibres is that they interrupt grain growth, leaving smaller grain sizes in the system, which allows the possibility of larger grain boundary diffusion paths. Furthermore, the presence of fibres introduces microstrain and further disorder in the structure according to the diffraction pattern analysis which is consistent with the observed changes in the DSC transitions as well as a number of the band shifts found in the ATR-FTIR spectrum. A decrease in the entropy of phase transition in DSC by fibre incorporation also indicates the development of disorder or amorphous phase formation in the structure. This may lead to the introduction of another mechanism for the ionic transport in the system; ion transport may occur along the disordered areas in the fibres/OIPC interface.

Lithium-doped [C_2mpyr][BF_4] incorporation within PVDF nanofibres

According to the XRD patterns, the PVDF fibres prevent the formation of the second phase in the lithium doped OIPC. This was supported by ^{19}F NMR data, which showed a change from two distinct ^{19}F resonances for lithium-doped OIPC into a homogenous environment in the lithium-doped composite, which suggests that all $[BF_4]^-$ anions exist in a single phase. As a result, the related phase transformation at 86 °C is not observed in the thermal traces of lithium-doped composites (fig. 2). According to the diffraction patterns, by introducing disorder into the lithium-doped system, the fibres prevent the formation of the high symmetry required for initiation of second phase nucleation. The absence of the new ring mode from the ATR-FTIR spectrum measured at room temperature also confirms that the second phase was not able to overcome the required energy barrier for its nucleation at low temperatures in this doped composite system. The absence of the second phase from the lithium-doped system brings significant changes in lithium ion and the anion dynamics. The mobility of both the Li ion and the anion is increased in a broad temperature range in phase II according to ^{7}Li and ^{19}F line width analysis (figs. 8c & 7b). In addition, the population of the mobile cation sites is increased in phase II according to ^{1}H spectra analysis (fig. 5c). The high temperature rotational motions of the cation are promoted at lower temperatures, which in turn facilitates greater lithium ion transport in the system in phase II. This explains the onset of narrowing of ^{7}Li spectra at temperatures below the phase II to I transition. This is also apparent from the calculated correlation time which indicates a significant increase in lithium ion diffusion in phase II. The suppression of the second phase formation in the composite releases additional numbers of lithium ions in the OIPC matrix structure, providing additional charge carriers in the system. The dissolved lithium ions may play an additional role in creating distortions in the solid solution structure as suggested by the increase in XRD peak widths, which can also be due to disordered areas in vicinity of fibres/Li-doped OIPC interfaces. All those structural changes provide additional sites for lithium ion hopping, thereby facilitating lithium ion transport. In addition, according to the correlation time analysis from VT-^{7}Li NMR measurements, lithium ions remain for a shorter duration at any given site suggesting an increased overall rate in the system (fig. 8d) and hence increased Li ion diffusion. All these changes result in a significant increase in ionic conductivity of phase II upon incorporation of fibres into the lithium doped system (fig. 3c). These results serve to provide a clear understanding of the electrolyte role in the previous demonstration of a lithium metal cell incorporating a lithium doped OIPC PVDF composite as the electrolyte that

functioned in phase II with a remarkably high level of performance[25]. The results of this study thus clearly show that the formation of a second, lithium rich phase results in poor lithium ion dynamics in the lithium doped OIPC in the absence of fibres, and hence the inability for a Li based device to operate in phase II.

Nevertheless, in the composite material, a decrease in both cation and anion mobility is observed compared to the neat lithium doped OIPC in phase I (figs. 4c & 7b), while Li ion dynamics remain relatively unchanged (figs. 8c & 8d). The population of the mobile cations are also reduced in phase I (fig. 5c). Therefore, a decrease in conductivity is observed in the lithium doped composite in phase I (fig. 3c). This may be due to fibre interaction with the lithium ions in phase I or because of the changes in the fibre chemistry at high temperatures. Vibrational spectroscopy and thermal gravimetric analysis (TGA) can provide additional information for the behaviour of the composite materials in this phase and this will form part of the scope of our future investigations.

Conclusion

In this study different scales of the $[C_2mpyr][BF_4]$ OIPC material were probed in pure and lithium-doped states and upon the incorporation of polymer nanofibres. The pure $[C_2mpyr][BF_4]$ undergoes several degrees of reorientation by increasing temperature towards phase I, resulting in the observation of different crystalline structures in each phase. The activation of new dynamics through these phase transitions establishes more degrees of freedom in the system, resulting in increased conductivity in the highly symmetric crystalline phase I.

Lithium addition results in the formation of an additional, presumably lithium rich phase. This second phase, which is observed at low temperatures, hinders ion dynamics in phase II resulting in lower ionic conductivity. This may be due to the formation of a blocking agent as an obstacle for ion diffusion through the bulk and grain boundary areas. Furthermore, the lithium ions are unable to contribute to conductivity as they are locked into a rigid phase. The gradual dissolution of the second phase, most likely as a solid solution inside the cubic structure of the material upon increasing temperature to phase I, releases a significant concentration of lithium ions as charge carriers in the system. This phenomenon, along with the removal of blocking agents in the system, significantly increases ion conductivity in moving towards phase I.

The polymer nanofibre incorporation into the pure OIPC system does not interrupt ion ordering within each crystalline phase. However, it introduces significant changes in the crystal structure by expanding the lattice, introducing defects, decreasing grain size and developing disorder within the structure. These effects result in activation of rotator sites at much lower temperatures than the equilibrium transition temperature along with significant growth in the population of rotating sites in the system. As a result an increase in ion conduction of the pure system is observed in both phase II and I by fibre incorporation. However, the degree of ion mobility is hindered in the presence of the fibres in both matrix and rotating phase of the material. This results in a retarding effect of the increase in ion conduction in phase I compared to phase II, although the increase in the number of mobile charge carriers brought about by fibre incorporation apparently dominates the conductivity behaviour in both phase I and II in this system.

Incorporation of the nanofibres in the lithium-doped system introduces significant changes in the properties of the Li-doped OIPC by avoiding the formation of the second phase along with the promotion of additional disorder. As a result Li-ion concentration as well as the mobility of both the lithium ion and the anion increases in the system. As a result a significant increase in ion conduction is observed in phase II, allowing the efficient operation of a lithium device in this phase, as previously reported.

Acknowledgements

The authors gratefully acknowledge financial support from the Australian Research Council (ARC) through the Australian Postgraduate Awards and Deakin University postgraduate research scholarships. This work was funded through the ARC Discovery program (grant DP140101535). The authors acknowledge support from ARC Centre of Excellence for Electromaterials Science (ACES). Prof. Maria Forsyth also acknowledges support from the Australian Laureate Fellowship (FL110100013) and for Deakin University's Magnetic Resonance Facility through LIEF program (grant LE110100141). An Australian Synchrotron beamtime allocation & SXRD beamline scientists (Dr. Justin Kimpton and Dr Helen Brand) are also acknowledged. The authors also wish to thank Dr. Jian Fang, Dr. Paul Bayley and Dr. Jim Efthimiadis (Deakin Univeristy, IFM) assistance with materials and characterization methods. The authors also acknowledge Dr. Anita Hill (CSIRO Manufacturing) for her support for the PALS measurements.

Keywords: Solid-state electrolyte, OIPC, lithium-doping, polymer, composite, ion mobility, defect, molecular interaction.

Notes and references

[a]ARC Centre of Excellence for Electromaterials Science (ACES), Deakin University, Burwood, Victoria 3125, Australia

[b]Institute for Frontier Materials (IFM), Centre for Chemistry and Biotechnology (CCB), Deakin University, Waurn Ponds, Victoria 3216, Australia

[c]Process Science & Engineering, Manufacturing, Commonwealth Scientific and Industrial Research Organisation, Clayton, VIC 3168, Australia

* Corresponding author: E-mail: Patrick.Howlett@deakin.edu.au; Fax: +61 3 9244 6868; Tel: +61 3 9244 5107

† Electronic Supplementary Information (ESI) available: [A supplementary file including: Synchrotron X-ray diffraction patterns in

different crystalline phases IV (-80°C), II (50°C) and I (100°C) for pure [C2mpyr][BF4] (S.1), pure [C2mpyr][BF4]/PVDF composite (S.2), lithium-doped [C2mpyr][BF4] (S.3) and lithium-doped [C2mpyr][BF4]/PVDF nanofibre composite (S.4) along with PALS results showing ortho-positronium lifetime variation with incorporation of PVDF nanofibre and by phase transition in pure [C2mpyr][BF4] (S.5)]. See DOI: 10.1039/b000000x/

1. Y. Abu-Lebdeh, A. Abouimrane, P.-J. Alarco and M. Armand, *Journal of Power Sources*, 2006, **154**, 255-261.
2. P. C. Howlett, J. Sunarso, Y. Shekibi, E. Wasser, L. Jin, D. R. MacFarlane and M. Forsyth, *Solid State Ionics*, 2011, **204-205**, 73-79.
3. P. C. Howlett, Y. Shekibi, D. R. MacFarlane and M. Forsyth, *Advanced engineering materials*, 2009, **11**, 1044-1048.
4. J. Sunarso, Y. Shekibi, J. Efthimiadis, L. Jin, J. M. Pringle, A. F. Hollenkamp, D. R. MacFarlane, M. Forsyth and P. C. Howlett, *Journal of solid state electrochemistry*, 2012, **16**, 1841-1848.
5. L. Jin, P. Howlett, J. Efthimiadis, M. Kar, D. Macfarlane and M. Forsyth, *Journal of materials chemistry*, 2011, **21**, 10171-10178.
6. L. Jin, K. M. Nairn, C. M. Forsyth, A. J. Seeber, D. R. MacFarlane, P. C. Howlett, M. Forsyth and J. M. Pringle, *Journal of the American Chemical Society*, 2012, **134**, 9688-9697.
7. D. R. MacFarlane, J. Huang and M. Forsyth, *Nature*, 1999, **402**, 792-794.
8. J. M. Pringle, *Physical Chemistry Chemical Physics*, 2013, **15**, 1339-1351.
9. P.-J. Alarco, Y. Abu-Lebdeh, N. Ravet and M. Armand, *Solid State Ionics*, 2004, **172**, 53-56.
10. W. A. Henderson, D. M. Seo, Q. Zhou, P. D. Boyle, J.-H. Shin, H. C. De Long, P. C. Trulove and S. Passerini, *Advanced Energy Materials*, 2012, **2**, 1343-1350.
11. Z.-B. Zhou and H. Matsumoto, *Electrochemistry Communications*, 2007, **9**, 1017-1022.
12. A. Hill, J. Huang, J. Efthimiadis, P. Meakin, M. Forsyth and D. MacFarlane, *Solid state ionics*, 2002, **154**, 119-124.
13. J. Efthimiadis, M. Forsyth and D. MacFarlane, *Journal of materials science*, 2003, **38**, 3293-3301.
14. J. Efthimiadis, G. Annat, J. Efthimiadis, D. Macfarlane and M. Forsyth, *Solid State Ionics*, 2006, **177**, 95-104.
15. Y. Shekibi, A. Gray-Weale, D. R. MacFarlane, A. J. Hill and M. Forsyth, *The Journal of Physical Chemistry C*, 2007, **111**, 11463-11468.
16. J. Adebahr, N. Ciccosillo, Y. Shekibi, D. Macfarlane, A. Hill and M. Forsyth, *Solid State Ionics*, 2006, **177**, 827-831.
17. Y. Shekibi, S. J. Pas, N. M. Rocher, B. R. Clare, A. J. Hill, D. R. MacFarlane and M. Forsyth, *Journal of Materials Chemistry*, 2009, **19**, 1635.
18. J. M. Pringle, Y. Shekibi, D. R. MacFarlane and M. Forsyth, *Electrochimica Acta*, 2010, **55**, 8847-8854.
19. Y. Shekibi, A. Gray-Weale, D. R. MacFarlane, A. J. Hill and M. Forsyth, *Journal of Physical Chemistry C*, 2007, **111**, 11463-11468.
20. S. Cavaliere, S. Subianto, I. Savych, D. J. Jones and J. Rozière, *Energy & Environmental Science*, 2011, **4**, 4761.
21. R. Sahay, P. S. Kumar, R. Sridhar, J. Sundaramurthy, J. Venugopal, S. G. Mhaisalkar and S. Ramakrishna, *Journal of Materials Chemistry*, 2012, **22**, 12953.
22. S. Ramakrishna, K. Fujihara, W.-E. Teo, T. Yong, Z. Ma and R. Ramaseshan, *Materials Today*, 2006, **9**, 40-50.
23. S. W. Choi, S. M. Jo, W. S. Lee and Y. R. Kim, *Advanced Materials*, 2003, **15**, 2027-2032.
24. Z.-M. Huang, Y. Z. Zhang, M. Kotaki and S. Ramakrishna, *Composites Science and Technology*, 2003, **63**, 2223-2253.
25. P. C. Howlett, F. Ponzio, J. Fang, T. Lin, L. Jin, N. Iranipour and J. Efthimiadis, *Physical Chemistry Chemical Physics*, 2013, **15**, 13784-13789.
26. Y. Shekibi, T. Rüther, J. Huang and A. F. Hollenkamp, *Physical Chemistry Chemical Physics*, 2012, **14**, 4597-4604.
27. J. Luo, O. Conrad and I. F. Vankelecom, *Journal of Materials Chemistry A*, 2013, **1**, 2238-2247.
28. W. A. Henderson, V. G. Young, S. Passerini, P. C. Trulove and H. C. De Long, *Chemistry of materials*, 2006, **18**, 934-938.
29. M. Forsyth, T. Chimdi, A. Seeber, D. Gunzelmann and P. C. Howlett, *Journal of Materials Chemistry A*, 2014, **2**, 3993-4003.
30. W. Henderson, V. Young Jr, W. Pearson, S. Passerini, H. De Long and P. Trulove, *Journal of Physics: Condensed Matter*, 2006, **18**, 10377.
31. A. Bielecki and D. P. Burum, *Journal of Magnetic Resonance, Series A*, 1995, **116**, 215-220.
32. D. Massiot, F. Fayon, M. Capron, I. King, S. Le Calve, B. Alonso, J. O. Durand, B. Bujoli, Z. Gan and G. Hoatson, *Magnetic Resonance in Chemistry*, 2002, **40**, 70-76.
33. N. Bloembergen, E. Purcell and R. Pound, *Phys Rev*, 1948, **73**, 679-712.
34. J. Kansy, *Nuclear Instruments and Methods in Physics Research Section A: Accelerators, Spectrometers, Detectors and Associated Equipment*, 1996, **374**, 235-244.
35. S. Tao, *The Journal of Chemical Physics*, 1972, **56**, 5499-5510.
36. M. Eldrup, D. Lightbody and J. Sherwood, *Chemical Physics*, 1981, **63**, 51-58.
37. W. A. Henderson and S. Passerini, *Chemistry of materials*, 2004, **16**, 2881-2885.
38. J. M. Pringle, J. Adebahr, D. R. MacFarlane and M. Forsyth, *Physical chemistry chemical physics*, 2010, **12**, 7234-7240.
39. S. A. Katsyuba, P. J. Dyson, E. E. Vandyukova, A. V. Chernova and A. Vidiš, *Helvetica chimica acta*, 2004, **87**, 2556-2565.
40. B. Bednarska-Bolek, R. Jakubas, G. Bator and J. Baran, *Journal of molecular structure*, 2002, **614**, 151-157.
41. H. W. Dudley and I. Fleming, *England: McGraw-Hill Publishing Company*, 1995, **16**.
42. P. Howlett, N. Brack, A. Hollenkamp, M. Forsyth and D. MacFarlane, *Journal of the electrochemical society*, 2006, **153**, A595-A606.
43. T. Enomoto, S. Kanematsu, K. Tsunashima, K. Matsumoto and R. Hagiwara, *Physical Chemistry Chemical Physics*, 2011, **13**, 12536-12544.
44. B. D. Cullity and S. R. Stock, *Elements of X-ray Diffraction*, Pearson, 2001.
45. F. Chen, H. Zhu and M. Forsyth, *ChemPhysChem*, 2014, **15**, 3530-3535.
46. H. Zhu, F. Chen, L. Jin, L. A. O'Dell and M. Forsyth, *ChemPhysChem*, 2014.
47. D. A. Porter and K. E. Easterling, *Phase Transformations in Metals and Alloys, (Revised Reprint)*, CRC press, 1992.
48. J. Efthimiadis, G. J. Annat, J. Efthimiadis, M. Forsyth and D. R. MacFarlane, *Physical chemistry chemical physics*, 2003, **5**, 5558-5564.
49. J. Huang, A. Hill, M. Forsyth, D. Macfarlane and A. Hollenkamp, *Solid State Ionics*, 2006, **177**, 2569-2573.
50. A. J. Hill, J. Huang, J. Efthimiadis, P. Meakin, M. Forsyth and D. R. MacFarlane, *Solid State Ionics*, 2002, **154–155**, 119-124.
51. R. Baughman and D. Turnbull, *Journal of Physics and Chemistry of Solids*, 1971, **32**, 1375-1394.

